Laser modified microstructures in ZrB_2, ZrB_2/SiC and ZrC

D.D. Jayaseelan [a,*], H. Jackson [a], E. Eakins [a], P. Brown [b], W.E. Lee [a]

[a] *Dept. of Materials, Imperial College London, South Kensington, London SW7 2AZ, UK*
[b] *Dstl, Porton Down, Salisbury, Wiltshire SP4 0JQ, UK*

Available online 10 April 2010

Abstract

Microstructural evolution of spark plasma sintered ZrB_2, ZrB_2/20 vol.% SiC (ZS20) and ZrC ultra high temperature ceramics (UHTCs) during laser heating has been investigated. Laser heating at temperatures between 2000 and 3750 °C for up to 300 s, in air or vacuum, resulted in extensive bubble and crater formation on the surfaces of 10 mm diameter samples. However, even after exposure to ultra high temperatures, samples did not disintegrate. X-ray diffraction of exposed faces of ZrB_2 and ZS20 samples laser heated in air up to 2700 °C detected only crystalline zirconia. A wide range of morphologies, including nodules, needles, nanofibres and lamella, were observed. The surface of ZrC samples, laser heated in vacuum up to 3750 °C, were characterised by dendritic and eutectic morphologies. Other features associated with melting, such as solidification cracks and trapped porosity, were also observed. A complex array of mechanisms involving solid, liquid and vapour phases led to formation of these various morphologies including melting, oxidation, volatilisation and liquid flow
Crown Copyright © 2010 Published by Elsevier Ltd. All rights reserved.

Keywords: Ultra high temperature ceramics; Laser heating; Microstructure; Oxidation; Melting; Electron microscopy

1. Introduction

Ultra high temperature ceramics (UHTCs), owing to their high melting temperatures and good chemical stability at elevated temperatures,[1–8] are being increasingly studied because of a growing need for materials that can operate in extreme aerothermal and nuclear power generation environments. For example, blunt leading edge components on the NASA space shuttle orbiter reach temperatures of around 2000 °C during atmospheric re-entry.[9] However, sharp leading edge hypersonic vehicle components, owing to much greater aerothermal heating, are expected to experience re-entry temperatures approaching 4000 °C. As a consequence, enhanced oxidation resistance is a key driver in the development of UHTCs for aero-propulsion and hypersonic flight applications. However, oxidation mechanisms for ZrB_2 and ZrB_2/SiC UHTCs above 1900 °C are not well understood[9–13] owing to their complexity and the difficulty of achieving such temperatures using conventional laboratory furnaces.

In terms of high temperature nuclear power generation, transition metal carbide UHTCs, such as ZrC, are attractive because of their low thermal neutron capture cross-section.[14] For example, ZrC could potentially be used in tri-structural isotropic (TRISO) reactor fuel as a dense barrier to prevent the release of harmful fission products whilst maximising fission transfer. However, in order to optimise the design of ZrC-based TRISO fuel a more complete understanding of the behaviour of ZrC at fission temperatures of 2000 °C, and above, is required. In particular, knowledge of how the thermo-physical and mechanical properties of ZrC vary with its stoichiometry is needed.

Laser heating/melting[14–18] offers several benefits over traditional methods for studying refractory materials, e.g. ultra high temperatures are readily and rapidly achieved and large test samples are not required. Moreover, laser surface modification (LSM) has emerged as a flexible and convenient technique for improving the surface properties of oxide ceramics including of porous alumina.[19–22]

The objectives of this paper are to demonstrate the feasibility of using laser heating techniques to study: (a) the oxidation characteristics of ZrB_2-based UHTCs in air at temperatures between 2000 and 3000 °C; (b) the thermo-physical behaviour of ZrC in vacuum at temperatures approaching 4000 °C; and (c) the surface microstructural evolution of non-oxide ceramics, i.e. Zr-based UHTCs.

* Corresponding author. Tel.: +44 0207 59 49 745.
  E-mail address: d.j.daniel@imperial.ac.uk (D.D. Jayaseelan).

2. Experimental details

2.1. Spark plasma sintering

ZrB$_2$ powder (>99%, $d_{50} \sim 2 \mu$m, Grade B, H.C. Starck, Newton, MA, USA), SiC powder (α-SiC, 98.5%, $d_{50} \sim 0.7 \mu$m, Grade UF-10, H.C. Starck, Newton, MA, USA) and ZrC (ABCR GmbH, Germany) were used as starting materials. Both ZrB$_2$ and α-SiC (6H) have a hexagonal structure with lattice parameters of $a = 3.17$ Å, $c = 3.53$ Å and $a = 3.08$ Å, $c = 15.12$ Å, respectively.

ZrC has a cubic symmetry with a rock salt structure and lattice parameter of 4.692 Å.[14] This is lower than the published value of 4.698 Å and can most likely be attributed to its higher impurity content. The commercial ZrC powders obtained from ABCR GmbH contained 11.18 wt.% C, 0.16 wt.% N, 0.51 wt.% O and 1.9 wt.% Hf, i.e. they were off-stoichiometric, ZrC$_{0.96}$.

Three systems, namely ZrB$_2$, ZrC and ZrB$_2$/20 vol.% SiC (ZS20) were prepared by spark plasma sintering using a furnace from FCT Systems, Germany. A 40 mm diameter die, lined with graphite foil, was used for ZrB$_2$ and ZS20 whereas a similarly lined 20 mm diameter die was used for ZrC. Graphite dies were also covered with graphite felt to reduce heat loss. Temperature was monitored by optical pyrometer. Samples were sintered between 1750 and 2000 °C for less than 5 min. A heating rate of 100 °C/min was maintained to the sintering temperature and an applied load of ~50 MPa was applied during sintering.

Monolithic ceramics were prepared directly from 'as-received' commercial powders. Composite ZS20 ceramics were fabricated from appropriate amounts of ZrB$_2$ and SiC which were wet ball milled and dried before sintering. Density measurements were conducted using the Archimedes method in water.

2.2. Laser heating

2.2.1. Defocused laser heating

Defocused laser (DFL) heating of ZrB$_2$ and ZS20 samples was carried out using a 3 kW Nd:YAG laser with a 10 mm diameter collimated beam capable of delivering a heat flux of up to ~20 MW/m^2. Sample temperature was recorded by a pyrometer (Raytek 1MH) with a measurement range of 650 and 3000 °C using a focus spot size of 1.7 mm at a standoff distance of 500 mm. The emissivity of ZrB$_2$ ceramics was assumed to be 0.73 as the actual emissivity was unknown. To obtain a close indication of temperature, pyrometer readings were taken at 0.2 s intervals (Fig. 1). After laser heating samples between 1750 and 3000 °C for up to 300 s the laser was turned off. The pyrometer reading immediately after this (T_{OFF}) was taken as being indicative of the temperature during DFL heating (T_{ON}). The example pyrometer temperature/time chart presented in Fig. 1 demonstrates that:
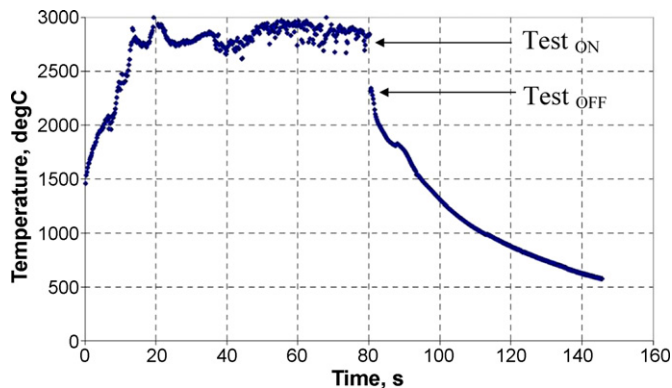
$$T_{ON} \approx T_{OFF} + 450 \,°C \tag{1}$$

Fig. 1. Pyrometer temperature recorded for heating ZrB$_2$ disc sample (20 s upslope then 60 s at 7.6 MW/m^2). Temperature uncertainty laser on and maximum temperature within 0.2 s of laser off was 2343 °C.

However the scatter in values of T_{ON}, connected with laser radiation/pyrometer interference, at ±150 °C, is significant. This was estimated to be ±5% for ZrB$_2$ and ZS20 at 2800 °C. To provide thermo-physical reference points, against which to compare recorded values of T_{ON}, samples were placed on a 0.55 mm thick piece of tantalum ($T_M \sim 3000$ °C) on top of a porous zirconica ($T_M \sim 2700$ °C) fire brick. For the DFL test corresponding to Fig. 1 the porous zirconia fire brick was observed to melt whereas the tantalum sheet remained solid. This indicates that 2700 °C < T_{ON} < 3000 °C which is consistent with an average pyrometer value for T_{ON} of ~2800 °C. Whilst estimates of T_{ON} obtained from the use of Eq. (1) are not precise they are informative, providing data that is sufficiently accurate to determine the temperature regime experienced by UHTC samples during DFL testing and also estimates of T_{ON} cannot be taken for granted as the measurement <2000 °C since the pyrometer may be sensitive enough to measure near accurate temperature. To avoid this discrepancy, T_{OFF} is quoted as measured temperature throughout the text. Whilst estimates of T_{ON} obtained from the use of Eq. (1) are not precise they are informative, providing data that is sufficiently accurate to determine the temperature regime experienced by UHTC samples during DFL testing. However, values of T_{OFF} have the advantage of being experimentally recorded data. Therefore, although it is probable that these values are too low by up to 450 °C, T_{OFF} is quoted as measured temperature throughout the text.

2.3. Laser melt testing

The laser melting apparatus used to characterise ZrC has been described previously by Manara et al.[15] Samples were held in a graphite fixture within a pressure vessel fitted with a sapphire window under 0.2 MPa argon. The use of this technique to characterise melting transition temperatures in ZrC has been described by Jackson et al.[14] A value of 0.6 was adopted as the best approximation for the high-temperature emissivity of ZrC, in accordance with typical values from the literature.[23] However, scattered and conflicting data introduce uncertainty into the reported temperatures. This was estimated to be ±1.5% for ZrC at 3000 °C.

2.4. Characterisation

Phase analysis of laser tested heated samples was carried out by X-ray diffraction (XRD) unit (Philips PW7100) using Cu Kα radiation. Plan view and cross-sections of the polished laser heated samples were observed under a scanning electron microscope (SEM) fitted with a field-emission gun (FEG, model LEO15) and energy dispersive spectroscopy (EDS) analysis was carried out for detection of elements. Detailed microstructural analysis was performed out using a JEOL 2000FX transmission electron microscope (TEM) operating at 200 kV with an Oxford Instruments microanalysis system on *ex situ* lift-out sections prepared by focus ion beam (FIB) sectioning in a FEI FIB200 operating with a gallium beam at 30 keV. Selected-area electron diffraction (SAED) patterns were acquired using a JEOL JEM-2000FX transmission electron microscope (TEM) and solved by the method of ratios.

3. Results

3.1. Sintered microstructures

Monolithic ZrB_2 sintered at relatively low temperatures (~1750 °C) with a holding time of 5 min attained only 92% of theoretical density (TD) whereas ZS20 X sintered for 5 min at 1900 °C attained 99% of TD and ZrC sintered for 5 min at 2000 °C was 96% of TD. Fig. 2 shows the surface microstructure of sintered samples. In monolithic ZrB_2 [Fig. 2(a)], no grain growth occurred on sintering but the microstructure contains many pores (<10 vol.%) and the average grain size is ~5.00 μm. Fig. 2(b) shows the dense microstructure of ZS20 comprising ZrB_2 (light phase) containing 20 vol.% SiC (dark phase). The SiC phase is interconnected and homogeneously distributed in the ZrB_2 matrix. The microstructure of chemically etched monolithic ZrC is shown in Fig. 2(c) and contains few pores (<1%) and has an average grain size ~10 μm.

3.2. Phase analysis

XRD confirmed that no phase transformation occurred in ZrB_2, ZS20 and ZrC after sintering. Images of ZrB_2 and ZS20 samples laser heated at a number of different temperatures are shown in Figs. 3 and 4, respectively. Although excessive bubble formation and melting were observed on the surface of ZrB_2 and ZS20 samples, they retained sharp edges and remained dimensionally stable to laser heating temperatures of ~2400 °C [Figs. 3(a)–(c) and 4(a)–(d)]. However, at higher temperatures, a porous crust formed on the surface in ZS20 laser heated at 2762 °C for 30 s [Fig. 4(e)]. ZS20 samples were also occasionally observed to spall when laser heated above ~2400 °C [Fig. 4(f)]. XRD of laser tested ZrB_2 (Fig. 5) and ZS20 (Fig. 6) samples revealed that all surfaces were covered with crystalline ZrO_2 phases. The intensity of m-ZrO_2 and c-ZrO_2 peaks increased with laser heating temperature whereas t-ZrO_2 decreased. During laser heating, ZrB_2 is known to start oxidising to ZrO_2 and liquid B_2O_3 at ~600 °C. Subsequently the liquid B_2O_3 evaporates as $B_2O_3(g)$ above 1000 °C.[24] However, newly
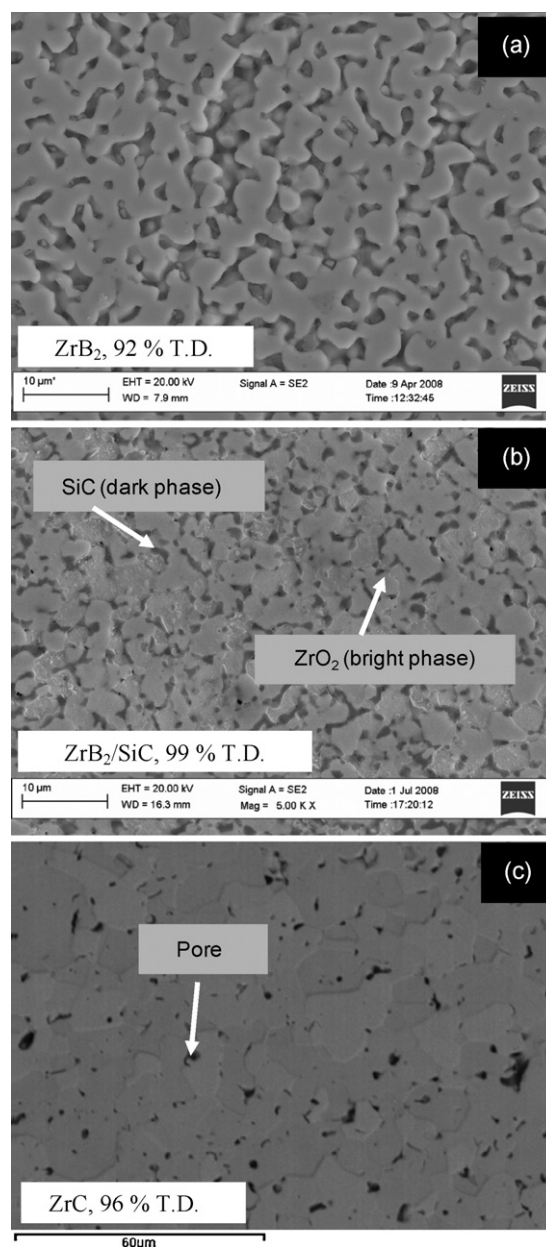

Fig. 2. Sintered microstructures of chemically etched UHTCs. (a) 92% dense monolithic ZrB_2 sintered at 1750 °C, (b) 99% dense ZrB_2/20 vol.% SiC sintered at 1900 °C showing homogeneous distribution of SiC in ZrB_2 matrix and (c) 96% dense monolithic ZrC showing uniform grain size.

formed monoclinic ZrO_2 undergoes successive transformation to tetragonal and cubic polymorphs on cooling. The unstabilised t-ZrO_2 transforms to m-ZrO_2 whereas fully stabilised c-ZrO_2 does not transform and hence all three crystalline forms of ZrO_2 were observed.

3.3. Laser modified microstructures

3.3.1. ZrB_2

Typical microstructures of laser heating ZrB_2 sample surfaces are shown in Fig. 7. After 120 s at 1781 °C [Fig. 7(a)], elongated grains with a diameter of ~1 μm and an aspect ratio of 5 are observed. EDS analysis showed these to be
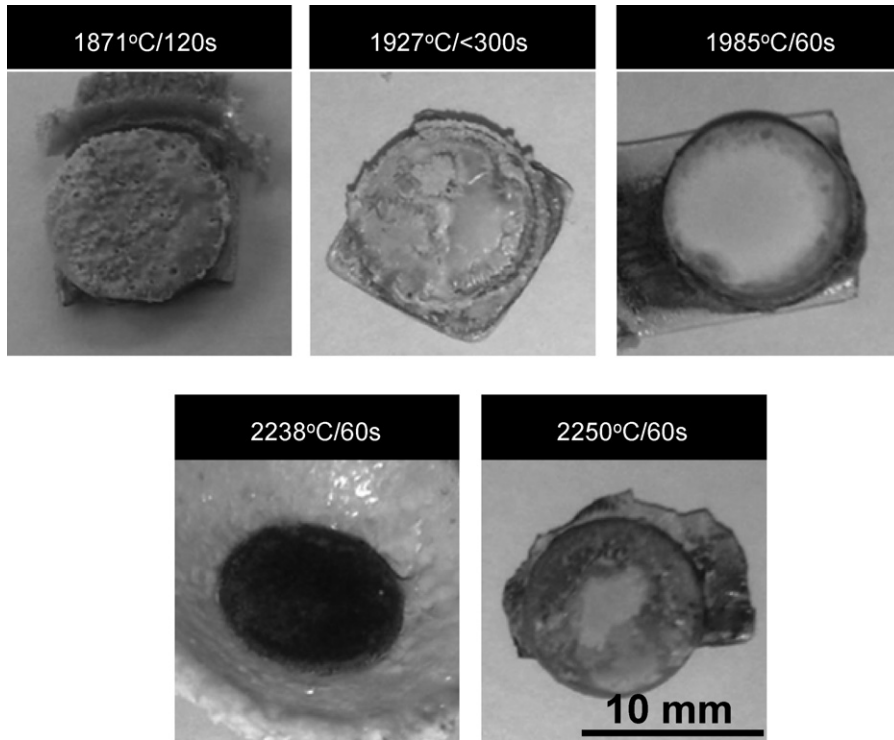
Fig. 3. Images of laser heated ZrB_2 samples after treatments indicated (All temperatures are T_{OFF} - see 2.2.1).

ZrO_2. Submicro- (<1 μm) and micro- (∼2 μm) cracks were also seen.

Fig. 7(b)–(d) shows the surface morphologies of ZrB_2 samples after laser heating for 300 s at 1927 °C using a DFL beam heat flux of 2.5 MW/m². The entire surface appears highly porous. Several different morphologies were observed in a single sample suggesting the operation of numerous oxidation mechanisms. Fig. 7(b) shows a porous network of highly faceted ZrO_2 grains with a diameter of ∼3 μm. However, Fig. 7(c) shows that smooth, oval ZrO_2 grains of a similar size were

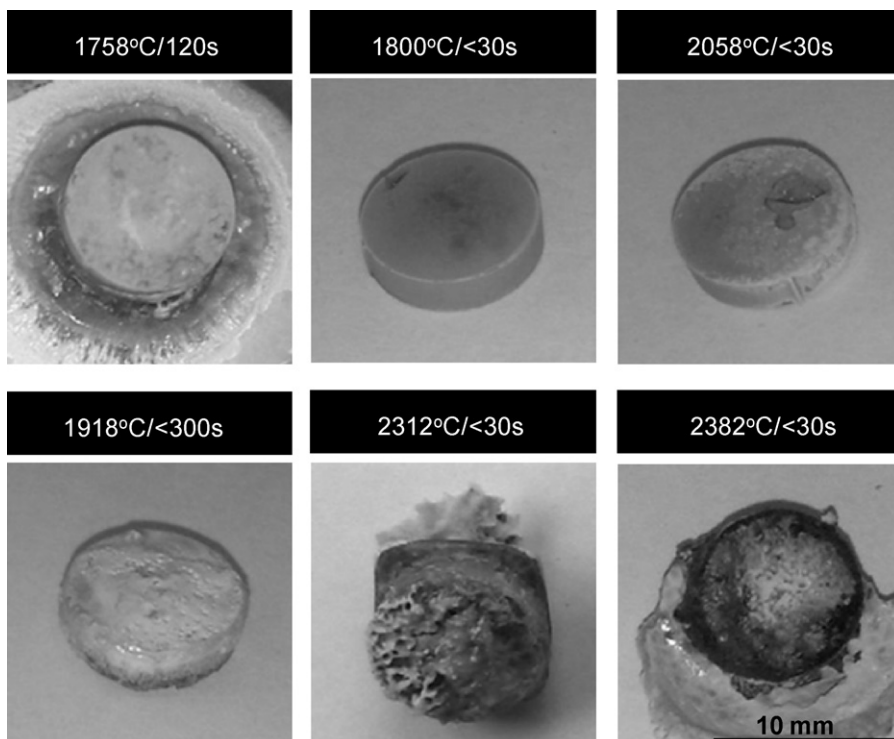Fig. 4. Images of laser heated ZrB_2/20 vol.% SiC samples after treatment indicated (All temperatures are T_{OFF} - see 2.2.1).
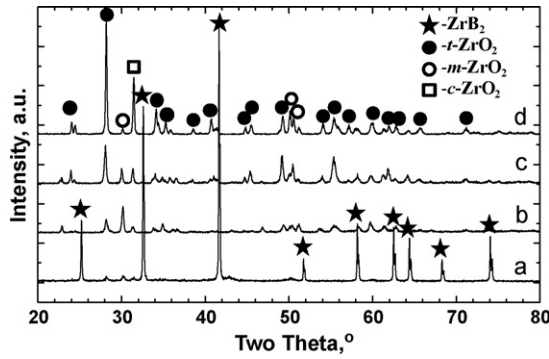
Fig. 5. XRD of laser heated ZrB_2: (a) untested, (b) 1871 °C, (c) 1927 °C and (d) 1985 °C (All temperatures are T_{OFF} - see 2.2.1).
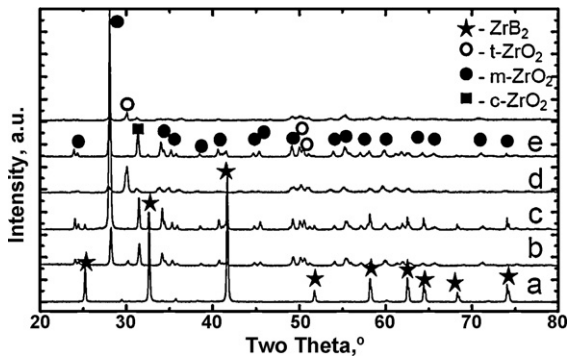

Fig. 6. XRD of laser heated ZrB_2/20 vol.% SiC: (a) untested, (b) 1725 °C, (c) 1800 °C, (d) 1918 °C, (e) 2058 °C and (f) 2312 °C (All temperatures are T_{OFF} - see 2.2.1).

also formed. Furthermore, both types of grain were surrounded by a 'web' structure comprised of ZrO_2 grains with a diameter of ~100 nm [Fig. 7(c)]. Nanofibres of ZrO_2 attached to the faceted surfaces of ZrO_2 shown in Fig. 7(b) were also observed [Fig. 7(d)].

Fig. 7(e)–(f) shows the modified surfaces of ZrB_2 laser heated for 300 s at 1954 °C using a DFL beam heat flux of 3.8 MW/m^2. A smooth dense outer layer can be seen in Fig. 7(e), containing cracks which probably arose from thermal stresses developed during rapid solidification on cooling. Fig. 7(f) shows the microstructure immediately below the outer layer of ZrO_2 which consists of florets of fibrous ZrO_2.

The surface of ZrB_2 after laser heating for 60 s at 1985 °C using a DFL beam heat flux of 3.8 MW/m^2 at low magnification (not shown) appears to be a smooth solid layer. However at higher magnification a highly porous ZrO_2 structure is revealed [Figs. 7(g) and (h)]. Clear evidence of the formation of a eutectic microstructure [Fig. 7(g)] and dendrite decoration of porous ZrO_2 grains was also observed [Fig. 7(h)].

Fig. 7(i) and (j) shows the outer surface features of monolithic ZrB_2 laser heated for 60 s at 2250 °C using a DFL beam heat flux of 3.8 MW/m^2. Two distinct features can be observed. Fig. 7(i) shows rapidly solidified, smooth ZrO_2 grains with inter- and intra-granular pores likely derived from the evolution of gaseous products. Fig. 7(j) shows formation of ZrO_2 needles, platelets and interlocking dendritic structures.

3.3.2. ZrB$_2$/20 vol.% SiC

Fig. 8 shows the surface laser modified ZS20 samples. After laser heating for 60 s at 1725 °C using a DFL beam heat flux of 3.8 MW/m^2, the ZS20 surface was covered with a smooth, continuous dark phase containing clusters of 100 nm nanoparticles [Fig. 8 (a)]. EDS analysis shows that the continuous phase consisted of Si and O whilst the nanoparticles consisted of Zr and O. Fig. 8 (b) shows the surface features of ZS20 after laser heating for 60 s at 1800 °C using a DFL beam heat flux of 3.8 MW/m^2. Nodular structures were observed on the surface.

The surface features of ZS20 after laser heating for 300 s at 1918 °C are seen in Figs. 8(c) and (d). A highly porous structure of interconnected ZrO_2 grains was observed in some areas, e.g. Fig. 8(c) whereas a dense microstructure with many macro-cracks and voids was observed in others, e.g. Fig. 8(d). These indicate shrinkage of the solidified melt during rapid cooling. The average grain size of ZrO_2 caused by laser refinement is <1 μm. Fig. 8(e) and (f) shows two distinct surface features of ZS20 after laser heating for 300 s at 1954 °C. The smooth surface in Fig. 8(f) arises from melt solidification on cooling and the rough porous surface in Fig. 8(e) is derived from evaporation of volatile gases whilst the melt is still liquid. Fig. 8(g) and (h) show the surface features of ZS20 after laser heating for 60 s at 2382 °C using a heat flux of 3.8 MW/m^2 consisting of a smooth melted surface containing nanopores [Fig. 8(g)] and smooth grains covered by a ZrO_2 web [Fig. 8(h)].

3.3.3. ZrC

Figs. 9–12 show the microstructures of laser melted ZrC. Fig. 9 shows the dendritic microstructure of the as-melted surface which was heated with a laser pulse using 3 mm diameter beam, ramped to peak power of 990 W in 50 ms, and held for a further 20 ms. The melted material was consistent with ZrC by XRD. A liquidus thermal arrest was detected in the cooling curve at 3350 °C, and the maximum temperature exceeded 3725 °C. Fig. 10(a) shows a cross-section through a second sample which was heated with four successive laser pulses using an 8 mm diameter beam, ramped to peak power of 2500–3800 W in 150 ms, and held for a further 250 ms. The top layer is the melted surface which consists of dense, homogeneous ZrC grains with a subsurface layer (C) characterised by primary ZrC grains along with pores and large bubbles whilst the bottom layer (B) is the un-affected ZrC.

Fig. 10(a) shows a cross-section of melted ZrC. Regions B and C in Fig. 10(a) are shown at high magnification in Figs. 10(b) and (c), respectively. No distinct features were observed on the top surface [Fig. 10(b)]. The observation of region C at high magnification [Fig. 10(c)] shows grains with different morphologies. Light contrast grains are ZrC surrounded by dark contrast ZrC + C eutectic phase. According to the published Zr–C phase diagram,[14] no ZrC + C eutectic phase exists at equilibrium for $ZrC_{0.96}$. Its presence is likely the result of fast quenching inhibiting homogenisation during freezing. Higher temperatures at the surface, together with repeated melting, enabled a single-phase ZrC layer to form. Bubbles and porosity are likely caused by
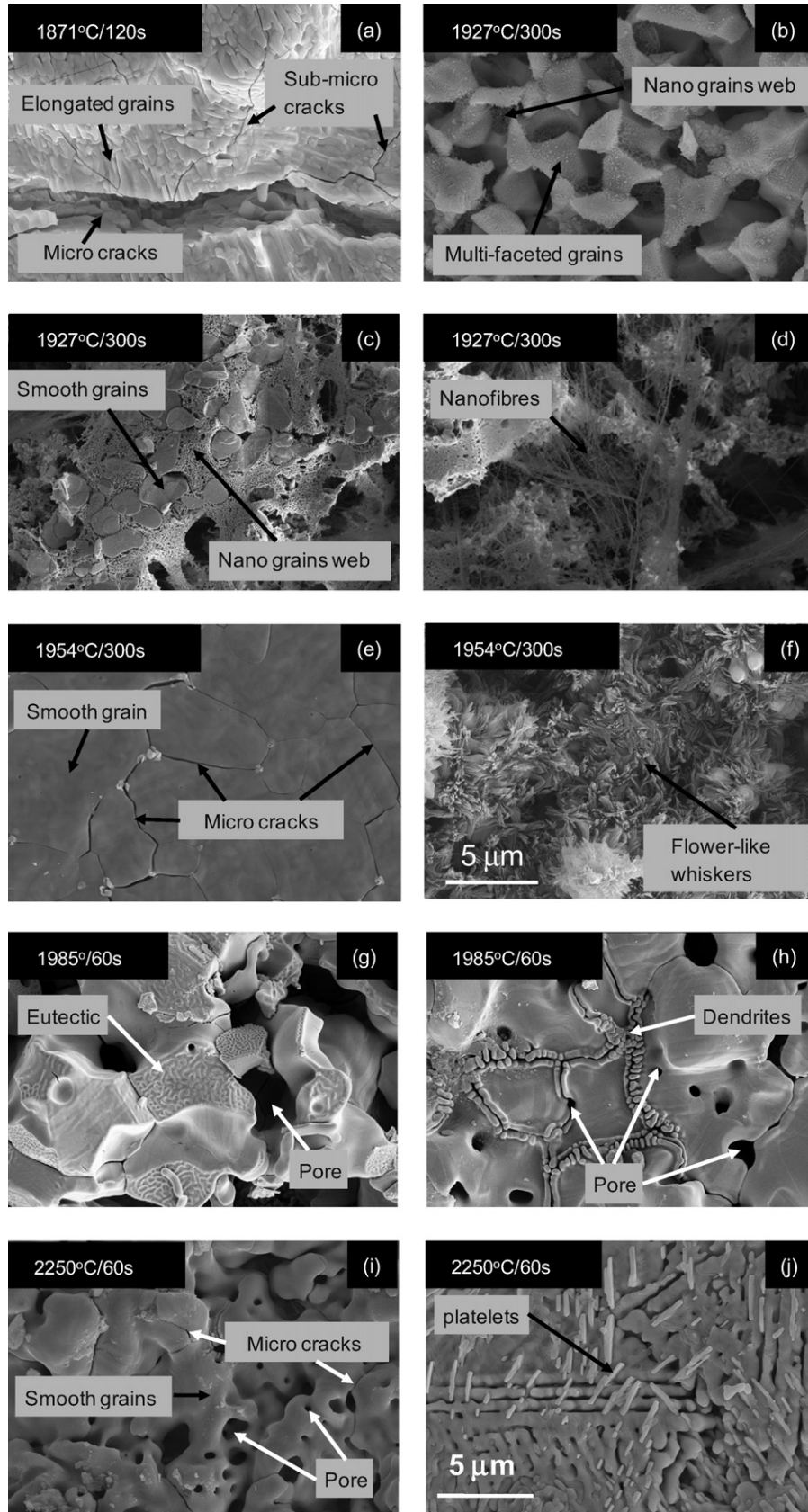
Fig. 7. Surface morphologies of laser heated ZrB$_2$ at (a) 1871 °C/120 s showing elongated grains and submicro- and macro-cracks; (b)–(d) 1927 °C/60 s showing different features including faceted smooth grains, nano-grain webs, and nanofibres in a single sample; (e) and (f) 1954 °C/300 s showing a smooth grained structure with micro-cracks and flower-like whiskers in single sample; (g) and (h) 2250 °C/60 s, showing eutectic, dendrites and inter-/intra-granular pores in a single sample; (i) and (j) 2250 °C/60 s, showing smooth grains, needles and platelets with micro-cracks and voids in a single sample (All temperatures are T_{OFF} - see 2.2.1).
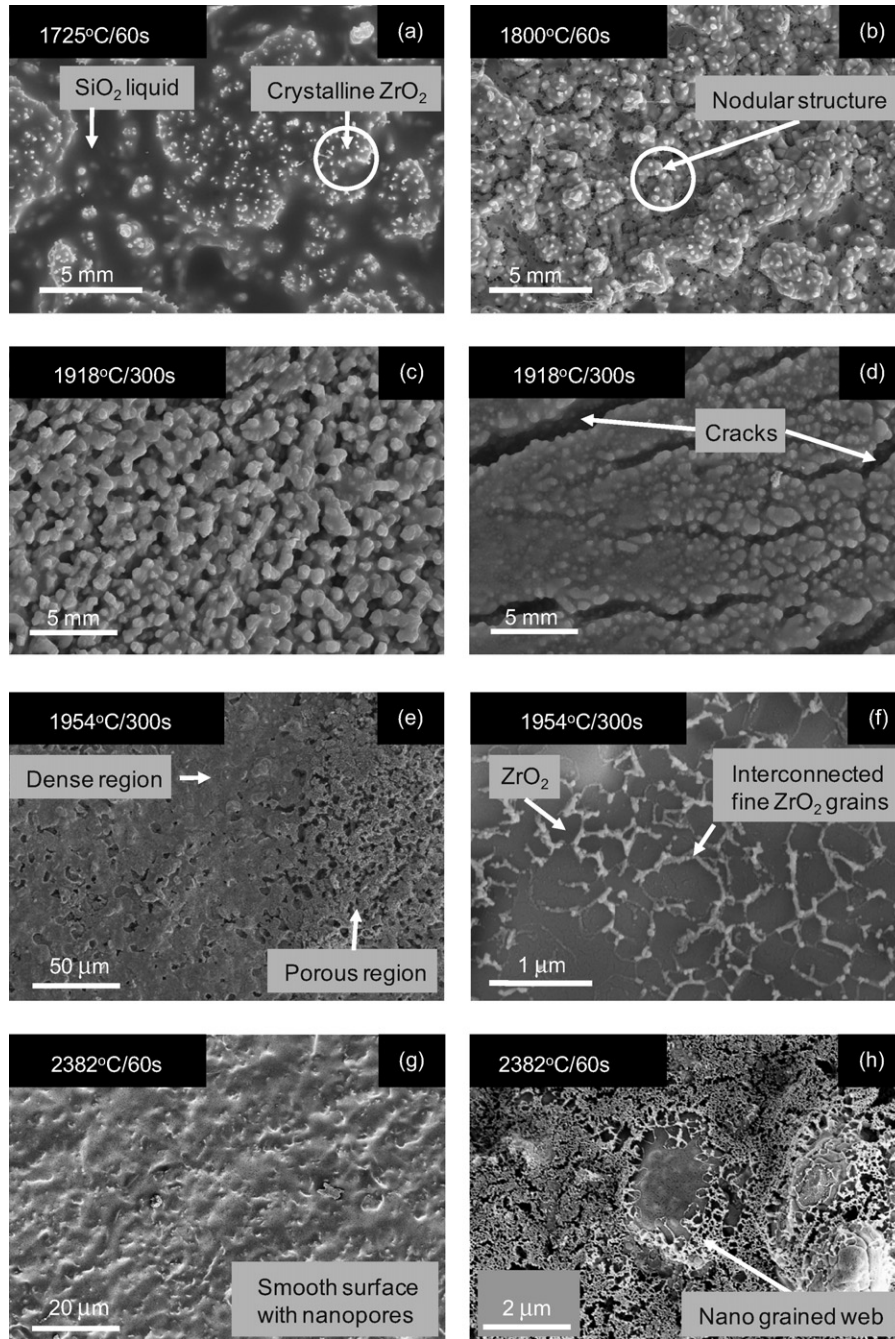
Fig. 8. Surface morphologies of laser heated ZrB$_2$/20 vol.% SiC at (a) 1725 °C/120 showing crystalline ZrO$_2$ grains surrounded by viscous SiO$_2$; (b) 1800 °C/60 s showing more crystalline ZrO$_2$ grains with nodular structure and little (<10%) viscous SiO$_2$; (c) and (d) 1918 °C/300 s showing two different features, highly porous region (c) and low porosity region with cracks (d) and no SiO$_2$ present but ZrO$_2$ surface grains, (e) and (f) 1954 °C/300 s showing different features in a single sample, highly porous and less porous regions and interconnected fine ZrO$_2$ grains on ZrO$_2$ surface and (g and h) 2382 °C/60 s showing different features such as smooth melted surface with nanopores and smooth grains covered with nano-grained ZrO$_2$ web on top (All temperatures are T_{OFF} - see 2.2.1).

substantial oxygen and nitrogen impurities in the starting ZrC (Section 2.1). Porosity is trapped below the surface because of freezing proceeding inward from the surface as well as outward from the bulk.

A bright-field TEM image of the microstructure of the eutectic region is presented in Fig. 11. Lighter C-rich and darker Zr-rich regions are distinguished by EDS. SADPs from the Zr-rich regions confirm it to be ZrC, having an fcc lattice with cell

parameter 4.7 ± 0.1 Å. The area analysed by electron diffraction consists solely of melted material. In Fig. 12, analysis of a C-rich region showed diffraction rings with streaks of increased intensity aligned linearly, indicating textured pyrolytic graphite. The d-spacing of the streaks was 3.3 Å, close to the spacing of graphite basal planes (3.35 Å). An underlying spot pattern associated with ZrC adjacent to the analysed region was also observed.
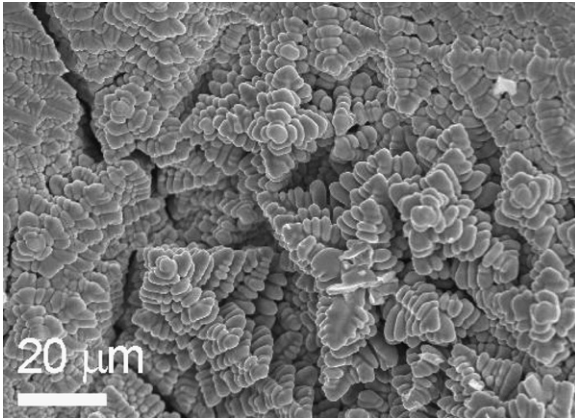
Fig. 9. Surface dendrites in laser melted ZrC at 3725 °C/70 ms.

4. Discussion

Sintered microstructures of UHTCs confirm that there is no appreciable grain growth after sintering even without sintering aids primarily because of the fast sintering rate used during SPS processing. The micrographs of ZrB_2, ZS20 and ZrC sample surfaces (Figs. 3 and 7–12) illustrate the modification of the virgin microstructures after laser heating: on the top of exposed faces, porous or dense oxide scales have formed in ZrB_2 and ZS20, and melting has occurred in ZrC.

The extensive bubbles and craters formed on the surfaces appear similar to those of volcanic outbursts. Liquid splashed out through cracks in the solidified crust under the pressure of gas that was liberated from the melt. The solidified melt did not splash out from all samples because sometimes the available amount of melt and the developed pressure of gas were only sufficient to open the crack further and fill the resultant space. Gases dissolved in the melt are liberated at the surfaces, and the high pressure developed in the cavity causes cracking of the outer crust and ejection of the melt from the region that has not yet crystallized.[25]

Microstructures of DFL-tested monolithic ZrB_2 indicate it has poor oxidation resistance at temperatures <2000 °C when compared to ZS20 composite primarily because of rapid volatilisation of B_2O_3 from it whereas passive protection of ZS20 occurs via highly viscous SiO_2. Above 2000 °C, as SiO_2 volatilises, SiC does not have any influence on oxidation. The exposed surfaces of DFL-tested samples show morphologies formed by different mechanisms. The exposed faces in all DFL-tested ZrB_2 and ZS20 samples remained porous except in a few regions. This is attributed to the evaporation of B_2O_3 and SiO_2 leaving behind porous ZrO_2.[26] However, at this temperature, the oxidised ZrO_2 grains coalesce to form a dense microstructure through liquid phase sintering and hence some regions of the exposed surface of DFL-tested ZrB_2 at 1871 °C are denser. The reason for the formation of smooth surfaces in DFL-tested samples at temperatures above 2000 °C is the occurrence of molten material (ZrO_2) and subsequent resolidification processes.[27] Pores and cracks arise from escape of volatile gases and shrinkage on solidification at high cooling rates, respectively.

Although B_2O_3 evaporation is faster at high temperatures (>1800 °C), there is a possibility of formation of transient boron–zirconium liquid along with crystalline ZrO_2:

$$ZrB_2 + (5/2)O_2 \rightarrow (1-x)(ZrO_2)_{crytalline}$$
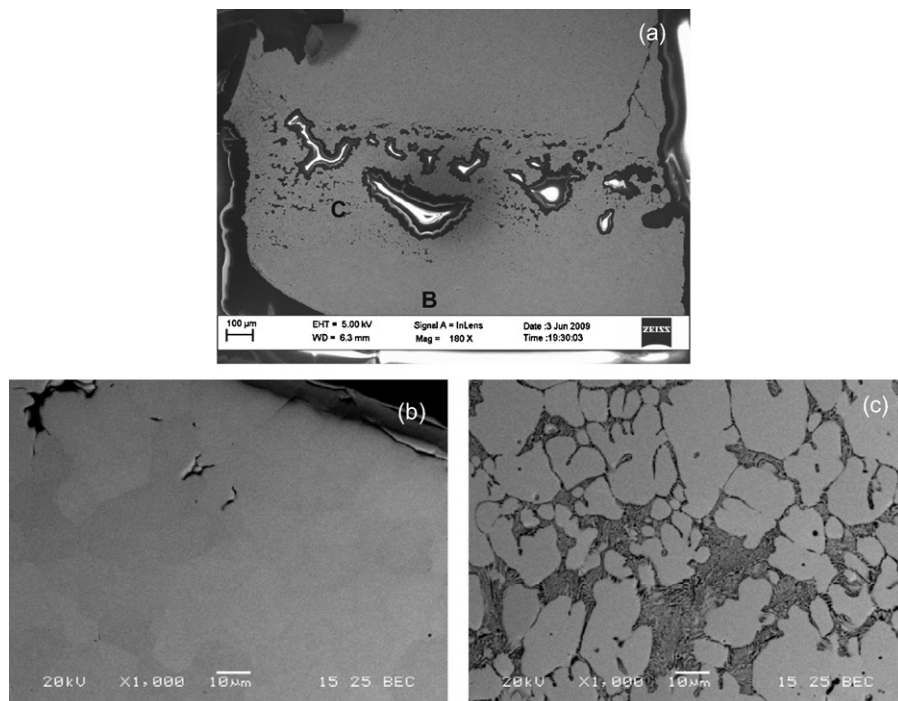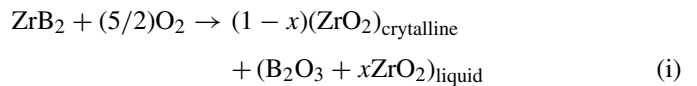$$+ (B_2O_3 + xZrO_2)_{liquid} \qquad (i)$$

Fig. 10. (a) Cross-section of melted ZrC, (b) high magnification of region B showing high density melted region and (c) high magnification of region C showing light contrast primary ZrC grains surrounded by dark contrast ZrC–C eutectic.
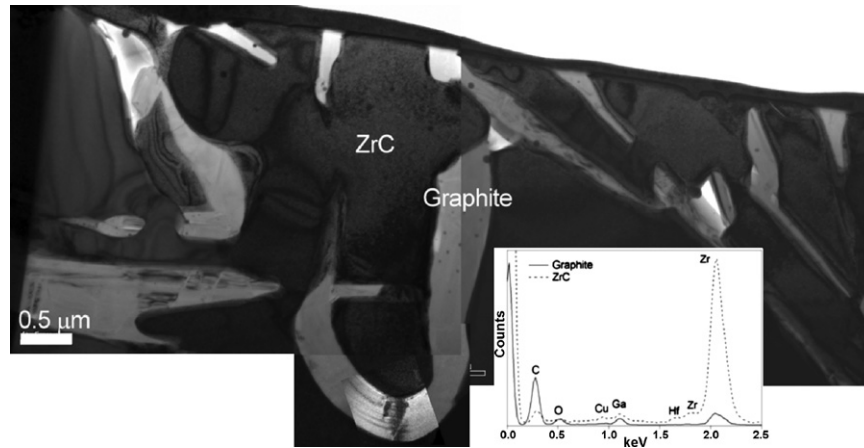
Fig. 11. A bright-field TEM image of the microstructure of the ZrC–C eutectic region.

At 1500 °C, the binary phase diagram[28] suggests that the mole fraction of primary zirconia is about 0.43 of the total composition, and the amount of (B_2O_3 + ZrO_2, BZ) liquid is about 0.57. The BZ liquid has a composition of 13 mol% dissolved ZrO_2 and 87 mol% B_2O_3. If all the B_2O_3 evaporates, the primary ZrO_2 would be 85 mol% and the precipitated secondary zirconia 15 mol% of the total solid ZrO_2.[28] Similarly, in the case of ZS20 >13 mol% ZrO_2 dissolves in BS liquid. Undissolved solid zirconia thus remains at the interface with ZrB_2 as the "primary zirconia",[29] whilst the BSZ liquid flows out to the surface, carrying dissolved zirconia. BSZ liquid can transport the dissolved zirconia to another location, where it might precipitate as zircon or as "secondary" zirconia.[29] Hence in almost all DFL-tested ZrB_2 and ZS20 samples, fine crystalline ZrO_2 particles (<1 μm) are observed on large (~5 μm) ZrO_2 grains.

Fig. 12. A bright-field TEM image and SADP of ZrC–C composite showing a textured polycrystalline pyrolytic graphite.

The formation of nanostructures such as needles, fibres, and faceted polygonal surface grains at the DFL-tested surfaces are a direct consequence of the rapid cooling rates associated with laser surface modification and associated effects on microstructure development. Whisker, needle and fibre morphologies are often associated with a growth mechanisms involving vapour.[30] The high temperatures encountered by these samples inevitably means that vapours are involved in the formation of the microstructures. Vapour transport and liquid/solid deposition leading to whisker/fibre/needle growth will be important in these ceramics. When the temperatures are sufficiently high, i.e. recorded as >2000 °C (the actual temperature must be at least 500 °C higher), melting of ZrO_2 (presumably "secondary" ZrO_2) should have occurred whilst B_2O_3 and SiO_2 volatilise. At high temperatures (>2000 °C), the interface between molten material on the top and bulk solid at the bottom provides the catalytic nucleation sites for heterogeneous nucleation and growth of the crystals. On further rapid cooling, they tend to grow with different morphologies. The dendritic microstructure confirms the presence of molten material on the surface which provides evidence that the oxidised product (ZrO_2) was molten at these temperatures confirming that the system was above the melting temperature of ZrO_2 (~2700 °C). Formation of nanofibres clearly indicates the involvement of vapour-phase reaction. The presence of the ZrC–C eutectic in DFL-tested ZrC suggests that either the liquidus was not reached or that rapid melting and quenching prevented the development of a homogeneous equilibrium phase. Formation of a dense, homogeneous surface layer was enhanced by higher surface temperatures and repeated melting.
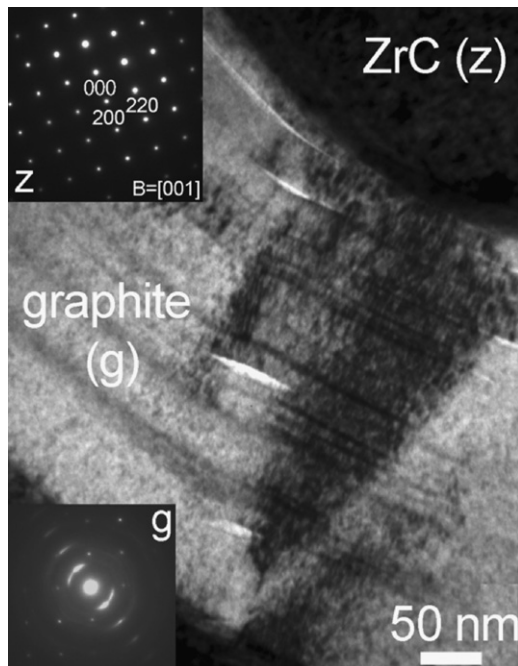
5. Conclusions

Laser heating of ZrB_2, ZrB_2/20 vol.% SiC and ZrC to temperatures of ~3000 °C led to formation of a range of microstructural features with morphologies such as needle-like nanostructures, dendrites, eutectic lamellae, nano-grained web and multifaceted polygonal surface grains. A complex array of solid–liquid–vapour-phase mechanisms were involved in the

formation of these features including melting, oxidation, volatilisation and liquid flow.

References

1. Chamberlain AL, Fahrenholtz WG, Hilmas GE. Low-temperature densification of zirconium diboride ceramics by reactive hot pressing. *J Am Ceram Soc* 2006;**89**:3638–45.
2. Licheri R, Orru R, Musa C, Cao G. Combination of SHS and SPS Techniques for fabrication of fully dense ZrB_2–ZrC–SiC composites. *Mater Lett* 2008;**62**(3):432–5.
3. Rezaie A, Fahrenholtz WG, Hilmas GE. Effect of hot pressing time and temperature on the microstructure and mechanical properties of ZrB_2–SiC. *J Mater Sci* 2007;**42**(8):2735–44.
4. Rezaie A, Fahrenholtz WG, Hilmas GE. Evolution of structure during the oxidation of zirconium diboride–silicon carbide in air up to 1500 °C. *J Eur Ceram Soc* 2007;**27**(6):2495–501.
5. Savino R, Fumo MD, Paterna D, Serpico M. Aerothermodynamic study of UHTC-based thermal protection systems. *Aerospace Sci Technol* 2005;**9**(2):151–60.
6. Wuchina E, Opila E, Fahrenholtz WG, Talmy IG. UHTCs: ultra-high temperature ceramic materials for extreme environment applications. *Interface* 2007;**16**(4).
7. Zhang SC, Hilmas GE, Fahrenholtz WG. Pressureless sintering of ZrB_2–SiC ceramics. *J Am Ceram Soc* 2008;**91**(1):26–32.
8. Zhu SZ, Xu Q, Feng C, Zhao JF, Cao JL, Wang FC. Effect of glass phase on the thermal shock resistance of ZrB_2–SiC ultra high temperature ceramic. *High Perform Ceram V, Pts 1 and 2* 2008;**368–372**:1727–9.
9. Marschall J, Erlich DC, Manning H, Duppler W, Ellerby D, Gasch M. Microhardness and high-velocity impact resistance of HfB_2/SiC and ZrB_2/SiC composites. *J Mater Sci* 2004;**39**(19):5959–68.
10. Medri V, Monteverde F, Balbo A, Bellosi A. Comparison of ZrB_2–ZrC–SiC composites fabricated by spark plasma sintering and hot-pressing. *Adv Eng Mater* 2005;**7**(3):159–63.
11. Bellosi A, Monteverde F. Ultra-refractory ceramics: the use of sintering aids to obtain microstructure control and properties improvement. *Eur Ceram Viii, Pts 1–3* 2004;**264–268**:787–92.
12. Opila E, Levine S, Lorincz J. Oxidation of ZrB_2- and HfB_2-based ultra-high temperature ceramics: effect of Ta additions. *J Mater Sci* 2004;**39**(19):5969–77.
13. Nguyen QN, Opila EJ, Robinson RC. Oxidation of ultrahigh temperature ceramics in water vapor. *J Electrochem Soc* 2004;**151**(10):B558–62.
14. Jackson HF, Jayaseelan DD, Clegge WJ, Reece MJ, Inam F, Manara D, et al. Laser melting of spark plasma sintered zirconium carbide: thermophysical properties of a generation IV very high temperature reactor material. In: *Proceedings of the 33rd international conference and exhibition on advanced ceramics and composites.* 2009.
15. Manara D, Pflieger R, Sheindlin M. Advances in the experimental determination of the uranium–oxygen phase diagram at high temperature. *Int J Thermophys* 2005;**26**(4):1193–206.
16. Welland MJ, Thompson WT, Lewis BJ, Manara D. Computer simulations of non-congruent melting of hyperstoichiometric uranium dioxide. *J Nucl Mater* 2009;**385**(2):358–63.
17. Belloni F, Manara D, Pflieger R, Colle JY, Rondinella VV. High-temperature thermodynamics by laser-vaporization mass spectrometry: an approach based on statistical mechanics. *Spectrochim Acta B-Atom Spectrosc* 2008;**63**(6):657–65.
18. Utton CA, De Bruycker F, Boboridis K, Jardin R, Noel H, Gueneau C, et al. Laser melting of uranium carbides. *J Nucl Mater* 2009;**385**(2):443–8.
19. Harimkar S. Effect of laser fluence on surface microstructure of alumina ceramic. *Adv Appl Ceram* 2006;**105**(6):304.
20. Samant AN, Harimkar SP, Dahotre NB. The laser surface modification of advanced ceramics: a modeling approach. *J Met* 2007;**59**(8):35–8.
21. Sartinska LL, Barchikovski S, Wagenda N, Rud BM, Timofeeva II. Laser induced modification of surface structures. *Appl Surf Sci* 2007;**253**(9):4295–9.
22. Zhang XH, Wang Z, Sun X, Han WB, Hong CQ. Thermal shocok behaviour of ZrB_2–20 vol.% SiC–15 vol.% graphite flake by hot pressing. *Int J Mod Phys B* 2009;**23**(6–7):1160–5.
23. Zapadaeva TE, Petrova VA, Sokolov VV. Emissivity of stoichiometric zirconium and titanium carbides at high temperatures. *High Temp* 1981;**19**.
24. Parthasarathy TA, Rapp RA, Opeka M, Kerans RJ. Effects of phase change and oxygen permeability in oxide scales on oxidation kinetics of ZrB_2 and HfB_2. *J Am Ceram Soc* 2009;**92**(5):1079–86.
25. Akopov FA, Valyano GE, Vorobev AY, Mineev VN, Petrov VA. Rapid solidification of ZrO_2–8 mol% Y_2O_3 melt. *High Temp* 2001;**39**(6).
26. Parthasarathy TA, Kerans RJ, Chellapilla S, Roy A. Analysis of ceramics toughened by non-conventional fiber reinforcement. *Mater Sci Eng A-Struct Mater Properties Microstruct Process* 2007;**443**(1–2):120–31.
27. Hontzopoulos E, Damigos E. Excimer laser surface treatment of bulk ceramics. *Appl Phys A: Solids Surf A* 1991;**52**.
28. Karlsdottir SN, Halloran JW, Grundy AN. Zirconia transport by liquid convection during oxidation of zirconium diboride–silicon carbide. *J Am Ceram Soc* 2008;**91**(1):272–7.
29. Karlsdottir SN, Halloran JW. Oxidation of ZrB_2–SiC: influence of SiC content on solid and liquid oxide phase formation. *J Am Ceram Soc* 2009;**92**(2):481–6.
30. Lee WE, Rainforth WM. *Ceramic microstructures—property control by processing.* London: Chapman and Hall; 1994.